Article

Structure

Atomic Resolution Cryo-EM Structure of β-Galactosidase

Graphical Abstract

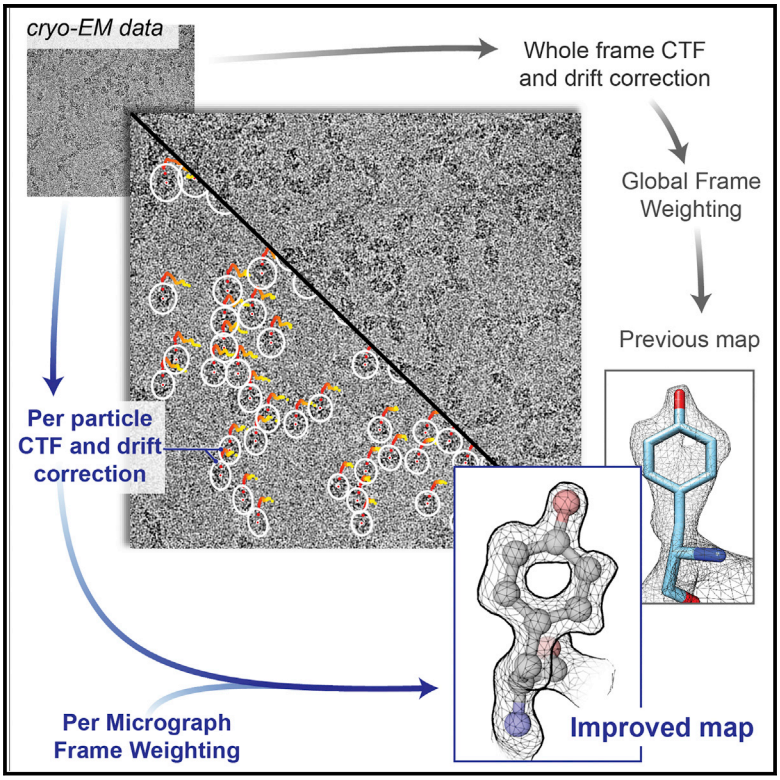

Highlights

- Improved methods for tracking particle movement during the electron exposure
- Atomic resolution cryo-EM map of inhibitor-bound β-galactosidase enzyme
- Delineation of spherical contours of non-hydrogen atoms and visualization of active site
- Evaluation of inhibitor flexibility using constrained molecular dynamics simulations

Authors

Alberto Bartesaghi, Cecilia Aguerrebere, Veronica Falconieri, ..., Guillermo Sapiro, Xiongwu Wu, Sriram Subramaniam

Correspondence

subramas@mail.nih.gov

In Brief

Bartesaghi et al. report methods to account for radiation damage and local changes in defocus and image drift, enabling visualization of atomic resolution features in a cryo-EM density map of inhibitor-bound β-galactosidase, and measuring of local flexibility of the bound inhibitor using constrained molecular dynamics simulations.

Bartesaghi et al., 2018, Structure *26*, 848–856
June 5, 2018 Published by Elsevier Ltd.
https://doi.org/10.1016/j.str.2018.04.004

CellPress

Structure
Article

Atomic Resolution Cryo-EM Structure of β-Galactosidase

Alberto Bartesaghi,[1] Cecilia Aguerrebere,[2] Veronica Falconieri,[1] Soojay Banerjee,[1] Lesley A. Earl,[1] Xing Zhu,[1] Nikolaus Grigorieff,[3] Jacqueline L.S. Milne,[1] Guillermo Sapiro,[2] Xiongwu Wu,[4] and Sriram Subramaniam[1,5,*]
[1]Laboratory of Cell Biology, Center for Cancer Research, National Cancer Institute, NIH, Bethesda, MD 20892, USA
[2]Department of Electrical and Computer Engineering, Duke University, Durham, NC 27708, USA
[3]Janelia Research Campus, Howard Hughes Medical Institute, Ashburn, VA 20147, USA
[4]Laboratory of Biophysical Chemistry, National Heart, Lung, and Blood Institute, NIH, Bethesda, MD 20892, USA
[5]Lead contact
*Correspondence: subramas@mail.nih.gov
https://doi.org/10.1016/j.str.2018.04.004

SUMMARY

The advent of direct electron detectors has enabled the routine use of single-particle cryo-electron microscopy (EM) approaches to determine structures of a variety of protein complexes at near-atomic resolution. Here, we report the development of methods to account for local variations in defocus and beam-induced drift, and the implementation of a data-driven dose compensation scheme that significantly improves the extraction of high-resolution information recorded during exposure of the specimen to the electron beam. These advances enable determination of a cryo-EM density map for β-galactosidase bound to the inhibitor phenylethyl β-D-thiogalactopyranoside where the ordered regions are resolved at a level of detail seen in X-ray maps at ∼ 1.5 Å resolution. Using this density map in conjunction with constrained molecular dynamics simulations provides a measure of the local flexibility of the non-covalently bound inhibitor and offers further opportunities for structure-guided inhibitor design.

INTRODUCTION

Improvements in the detective quantum efficiency of direct electron detectors combined with their ability to operate in movie mode have created unique opportunities for the development of computational strategies in single-particle cryo-electron microscopy (EM) capable of achieving unprecedented resolutions. By harnessing the time-resolved information contained in movie frames, these techniques have managed to overcome fundamental resolution barriers inherent to imaging biological samples using high-energy electrons. There are three main areas where improvements in data processing have been made thus far: (1) strategies to account for beam-induced motion or stage drift during the electron exposure (Abrishami et al., 2015; Bartesaghi et al., 2014; Brilot et al., 2012; Grant and Grigorieff, 2015; Rubinstein and Brubaker, 2015; Scheres, 2014; Zheng et al., 2017), (2) strategies to improve the accuracy of contrast transfer function (CTF) estimation using data from individual frames (Bartesaghi et al., 2014; McMullan et al., 2015; Rohou and Grigorieff, 2015; Zhang, 2016), and (3) development of exposure weighting schemes to compensate for radiation damage effects (Grant and Grigorieff, 2015; Rubinstein and Brubaker, 2015; Scheres, 2014; Zheng et al., 2017). Despite these advances, the accurate estimation of CTF parameters and alignment of movie frames on a per particle basis remains a challenging problem due to the combination of poor signal-to-noise ratios (SNRs) resulting from the low accumulated doses in each frame (typically below one electron per Å^2) and the small image area occupied by single particles. In addition, the inability of existing exposure compensation strategies to capture the highest resolution data recorded during the earliest part of the exposure remains a major resolution-limiting factor (Glaeser, 2016).

A second aspect of our work addresses the level of precision in determining the structures of ligands bound non-covalently to proteins. Of the 63 entries presently reported in the Electron Microscopy Data Bank of structures of protein complexes smaller than 1 MDa at resolutions better than 3.5 Å, 22 entries also report visualization of bound ligands (emdatabank.org). Interestingly, in almost all of these high-resolution cryo-EM density maps that include densities for bound ligands, the latter densities are typically at lower resolution than in ordered regions of the protein. Establishing the most effective way of utilizing structural information from deposited density maps is critical when cryo-EM structures are used in the context of structure-guided drug design, especially when no comparable structures are available from X-ray crystallography, and ligands may have weak affinity. If the lower resolution of the bound inhibitor densities arises solely because of the lower overall map resolutions, one approach to achieve better ligand definition would be to improve the resolution of the overall map to resolutions much higher than 2 Å so that bound inhibitors could be visualized at resolutions in the range of ∼2–2.5 Å, which are necessary for their use in rational drug design. Alternatively, if the resolution in cryo-EM density maps were limited primarily by intrinsic thermal flexibility of non-covalently bound weak inhibitors, alternative computational approaches would need to be explored to extract useful additional structural information on the inhibitor for purposes of improving compound efficacy.

In the work presented here, we report the development of advanced image processing methods that enable us to further

improve the resolution of the cryo-EM density map of β-galactosidase. We also take advantage of the improved resolution to extract additional information on the local flexibility of the bound inhibitor using molecular dynamics simulations.

RESULTS

Per Particle Analysis and Exposure Weighting

To evaluate whether map resolutions could indeed be improved further and to test their effect on improving ligand resolution, we carried out structural analysis of the enzyme β-galactosidase bound to the inhibitor phenylethyl β-D-thiogalactopyranoside (PETG) for which we had previously reported a structure at ~2.2 Å resolution (Bartesaghi et al., 2015). The density for the inhibitor in this map is weaker than that of residues in the active site and only adequate to position it approximately in its binding site. To improve overall map resolution, we implemented an approach with three distinct elements: (1) a strategy for local, per particle drift correction to follow the trajectory of individual particles throughout the exposure to the electron beam; (2) the use of local defocus estimation to track spatial CTF variations across the field of view; and, most importantly, (3) the use of a data-driven exposure compensation scheme that optimally weights the contribution of movie frames on a per micrograph basis. All underlying image alignment operations were carried out using a completely rewritten version of the program FREALIGN (Grigorieff, 2016), which uses a matched filter (McDonough and Whalen, 1995) to align particle images.

The use of methods for local drift correction combined with local CTF estimation provides assessment of the movement of each particle during the exposure in addition to a measure of the defocus and astigmatism variation across the image (Figures 1A–1C). From these measurements, we derived a correlation score for every particle in every frame (an indicator of the quality of the match between the raw movie data and re-projections of the three-dimensional [3D] reference), and carried out statistical analysis of the scores and their variances. Even though the individual measurements are noisy, we noticed that averaging score values across all particles in a micrograph (Figure 1D) consistently produced characteristic bell-shaped curves that peaked toward the early part of the exposure (where the SNR at high resolution is maximized), followed by a continuous decay toward the end of the exposure consistent with the onset of radiation damage (Baker et al., 2010). Interestingly, analysis of the average score distribution across all micrographs in the dataset showed a higher variance at the beginning of the exposure (Figure S1A), revealing considerable variations in image quality during the early frames in contrast with the more systematic effects of radiation damage observed in later frames. For example, we noted that micrographs with large initial movements had lower scores during the early frames (Figure S1B), compared with micrographs that had less drift at the beginning of the exposure. This is consistent with the fact that rapid specimen movement can result in blurring of the high-resolution information contained within a single frame. Taken together, these observations indicate that per micrograph score averages are consistent indicators of image quality, and as such can be used to weight the contribution of individual frames, allowing more effective capture of the high-resolution information present within the exposure.

Resolution Improvements with Proposed Correction Scheme

To verify the effectiveness of each component in our processing strategy, we applied the local defocus, local drift, and exposure weighting strategies separately and individually assessed improvement in map quality for each step, with respect to a reconstruction obtained using global motion correction, global CTF estimation, and the full exposure. Fourier shell correlation (FSC) values between half-maps provide an internally consistent measure to assess relative improvements in map quality achieved with each of these steps. Using this criterion, we show that there are measurable improvements in resolution of 0.07 Å, 0.09 Å, and 0.12 Å when we apply corrections for local defocus, local drift, and exposure weighting, respectively (Figure S1C). The fact that changes observed in the FSCs are all above the highest resolution used for refinement (see STAR Methods) validates the use of this metric as a reliable indicator of map quality that is not prone to overfitting. The combined effect of all three components resulted in a significantly improved density map with an overall resolution improvement of 0.4 Å (Figures 2, S1D, and Video S1). The new map shows delineation of the contours for non-H atoms as well as clear density for side chains such as lysine and arginine that faithfully follow the kinks in the extended side chains.

A qualitative approach to assessing map quality is shown in Figure S2, where we show a side-by-side comparison of a 2Fo-Fc map of β-galactosidase computed from the X-ray structure reported at 1.7Å resolution (PDB ID 1DP0) and the present map. The new map compares favorably against the 1.7Å resolution X-ray structure, as shown by visualization of the density in a stretch of residues (451–457, Figure S2A) and examples of the 20 amino acids (Figure S2B). Comparison of cryo-EM maps (which are derived without any use of an atomic model) and 2Fo-Fc maps (derived using model phases) can lead to an underestimate of the resolution of the cryo-EM maps because knowledge of exact phase information from the model eliminates noise that is present when phases are obtained experimentally, as is the case with cryo-EM maps. To make a more meaningful comparison, we also show examples of X-ray crystallographic maps obtained using single-wavelength anomalous diffraction that only use experimental phase information and are not biased by phases derived from an atomic model. Inspection of density contours for non-H atoms in these maps shows that the highest resolution features observed in our new cryo-EM density map of β-galactosidase are at higher resolution than in the 1.8 Å map of sedolisin (Wlodawer et al., 2017), and compare favorably with those seen in the 1.5 Å electron density map of insulin (kindly provided by Dr. Alex Wlodawer; Figure S3).

Next, we evaluated a variety of approaches to define the resolution of the map on a quantitative basis. Measures of resolution in cryo-EM maps typically involve the use of FSC plots, and we first provide some background to the different ways in which these plots are used. A commonly used FSC plot measures the self-consistency between two independent halves of the data and assigns the value at FSC of 0.143 as the nominal resolution (Rosenthal and Henderson, 2003; Harauz and van Heel, 1986). A different measure of map quality is to compute the FSC values between the map and the density calculated from

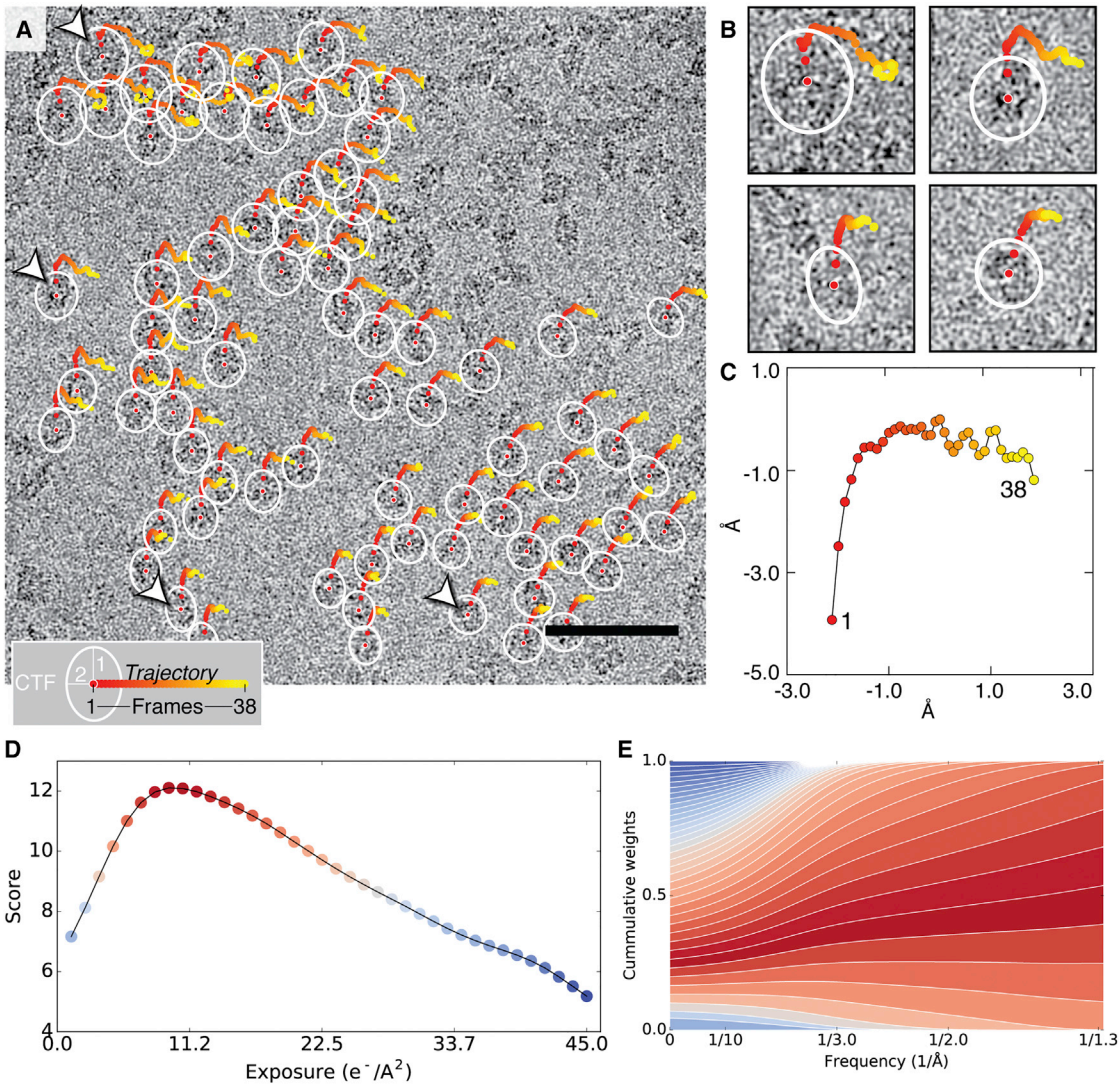

Figure 1. Per Particle Drift Movement, Local CTF Estimation and Exposure Weighting

(A) Trajectories of individual particles from micrograph EMD-2984_0925 start at the center of the white ellipsoidal markers and range from red (first frame) to yellow (last frame). Defocus changes across the field of view are typically small and were encoded as follows to improve visualization: mean ellipse radius is proportional to the average defocus (DF1+DF2)/2 and ellipticity is proportional to the amount of astigmatism difference measured at the location of each particle with respect to the global astigmatism value. Scale bar represents 50 nm.

(B) Zoomed-in view of selected particles indicated by arrowheads in (A).

(C) Global drift trajectory obtained by averaging all local particle trajectories in this micrograph.

(D) Average FREALIGN score computed over all particles in each frame plotted as a function of the cumulative electron dose. High scores are shown in red and low scores in blue.

(E) Corresponding two-dimensional weights showing the relative contribution of each frame to the weighted average as a function of spatial frequency; color scheme as in (D).

Related to Figure S1.

the atomic model. The highest resolution where there is positive correlation could be construed as an upper limit of the information content present in the map, although the resolution at which the FSC has a value of 0.5 is generally used as an indication of map resolution. The map versus model FSC plot is in principle a more absolute measure of resolution than the half-map FSC plots, but at high resolutions there are factors that lead to differences between maps computed from atomic models and maps obtained from cryo-EM, including inaccuracies in the modeling of radiation damage effects and imprecisions in the determination of electron scattering factors (Grigorieff et al., 1996).

For both kinds of FSC plots, the mask used to pre-multiply the maps before computing the correlation values is an important factor that determines the profile of the FSC plot (Chen et al., 2013). Because the resolution is typically higher in the central and more ordered regions of the protein, a mask that includes the entire protein provides an average value that underestimates the resolution in the more ordered regions, while tighter shape

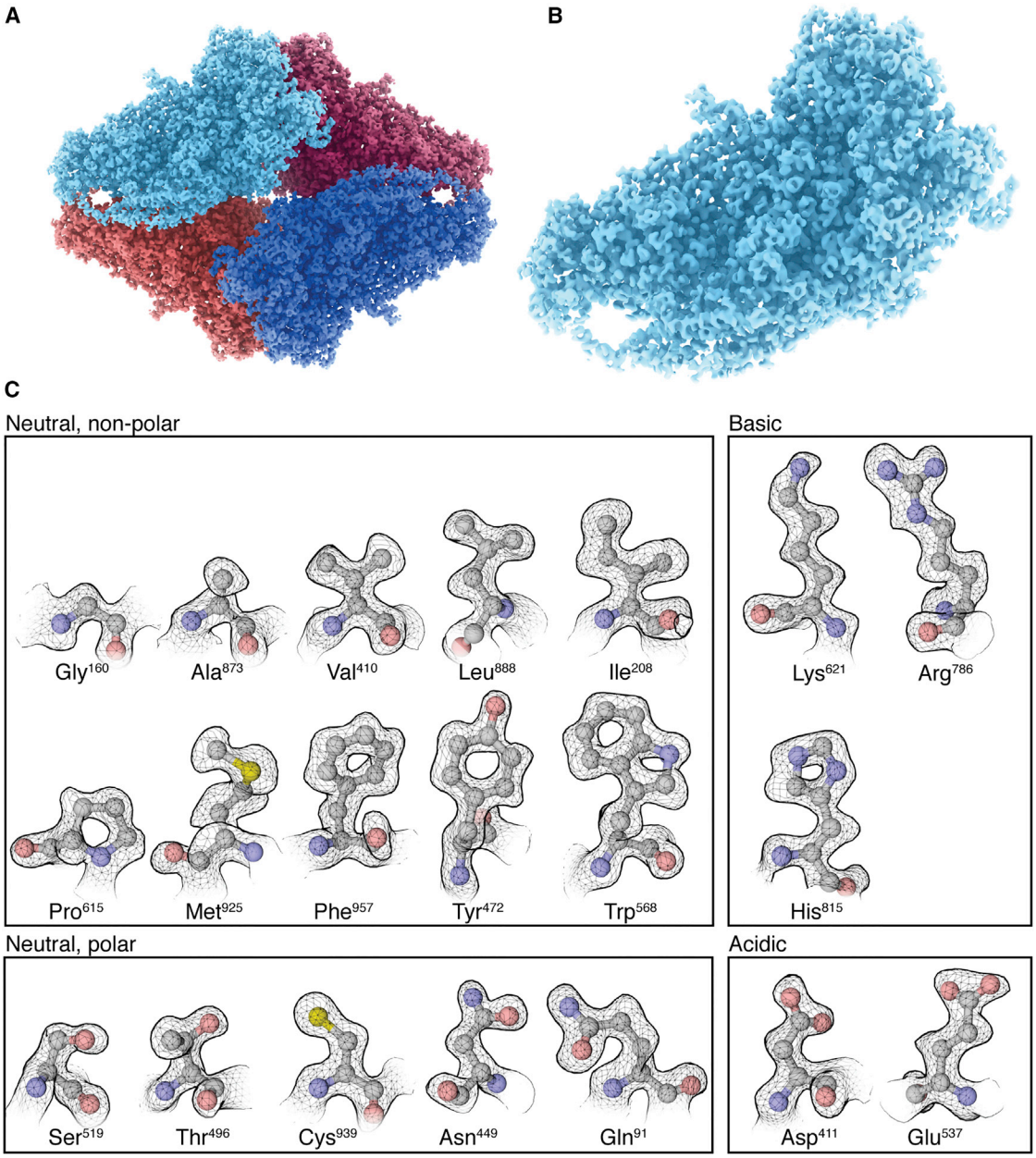

Figure 2. Cryo-EM Map and Visualization of Atomic Resolution Features

(A and B) Overview of β-galactosidase tetramer (A) and detailed view of asymmetric unit (B).

(C) Gallery of selected residues for each of the 20 amino acids showing delineation of the contours for non-H atoms as discrete, punctate features and clear density for side chains such as lysine and arginine that faithfully follow the kinks in the extended side chains.

Related to Figures S1–S4 and Video S1.

masks that exclude the periphery of the protein provide a measure of the resolution of the more ordered regions. A particular and useful version of masking is to estimate local resolution in each sub-region of the map; programs such as RESMAP (Kucukelbir et al., 2014) or BLOCRES (Cardone et al., 2013) provide plots of this spatial variation in resolution. We estimated resolution of our map using all of these different measures. The half-map FSC and the model versus map FSC plots show values of ~1.9 Å (0.143 cutoff) and ~2.1 Å (0.5 cutoff) with masks that include the entire protein. Plots of the spatial variation of the FSC using BLOCRES show an average resolution of ~1.8 Å with values ranging from 2.2 Å to 1.4 Å across different regions of the protein (Figure S1E), consistent with the visualization of distinctive atomic resolution features in the map.

Comparison with Previous Cryo-EM Density Maps

The density map presented in Figure 2 was obtained using the same data used to obtain the map we previously reported at

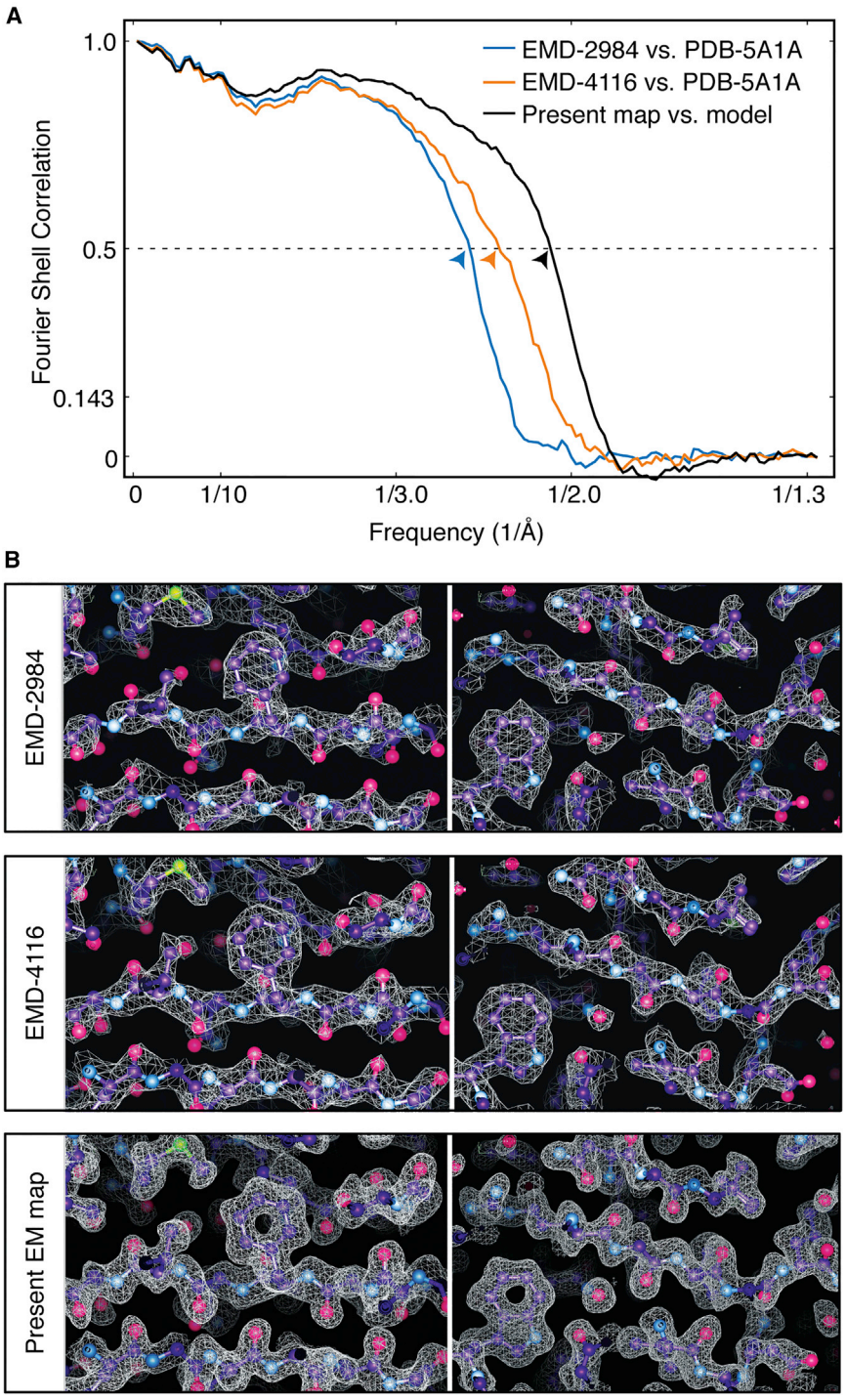

Figure 3. Comparison with Density Maps of β-Galactosidase Obtained from EMPIAR-10061

(A) FSC plots of map against atomic model for our original map (EMD-2984), the one obtained by Kimanius et al. (2016) using RELION (EMD-4116), and the present map, showing resolution improvements compared with the original map of ~0.2 Å and ~0.5 Å (corresponding with 0.5-FSC cutoffs of ~2.6 Å, ~2.4 Å, and ~2.1 Å, respectively). The mask used for the FSC calculations includes the entire protein and is the same one used by Kimanius et al. (2016) (part of the EMD-4116 entry). All maps were pre-multiplied by this mask before calculation of the FSC curves using EMAN2 (e2proc3d.py –calcfsc option).

(B) Side-by-side comparison of regions surrounding residues 957 (left) and 353 (right) from the three maps, showing corresponding improvements in map appearance.

Related to Figure S4.

2.2 Å resolution (Bartesaghi et al., 2015), publicly available in the EMPIAR database (entry 10061). Our original map was derived from ~40,000 particles, used whole-frame alignment, and only an early portion of the exposure (frames 4–13) based on the determination that these frames had the greatest amount of high-resolution information. More recently, Kimanius et al. (2016) used the program RELION to obtain a 3D reconstruction from the same set of deposited images but extracted almost three times as many particles (~110,000) from the same dataset. They also applied a "particle-polishing" procedure (Scheres, 2014), which enables accounting for the movement of individual particles during exposure to the electron beam and implements an exposure weighting scheme using information derived from the relative contribution of each frame to the reconstruction. A direct comparison of the features observed in our earlier map and the map obtained by RELION (also at a reported resolution of 2.2 Å) is presented in Figure S4, using the same panel of 20 amino acids presented in Figure 4 of Bartesaghi et al. (2015) as a reference. There is no significant difference in the appearance of the two maps by this measure, which is reflective of the best-resolved regions of the map. However, model versus map FSC plots (using an identical mask that includes the entire protein in both cases) shows an improvement in resolution of 0.2 Å in the RELION-derived map (Figure 3A). Factors contributing to the improvement of the RELION-derived map include the use of a much larger (~3×) particle stack, the corrections for local drift and relative weighting of frames present in the exposure, and potentially other aspects unique to the use of maximum likelihood methods during refinement and reconstruction (Cheng et al., 2015). Calculating FSC plots using the same mask as before shows that the resolution of the map we report here is improved by 0.5 Å compared with our previous map (Figure 3A). This quantitative improvement in resolution reported by the FSC curves of map versus model is consistent with the enhanced appearance

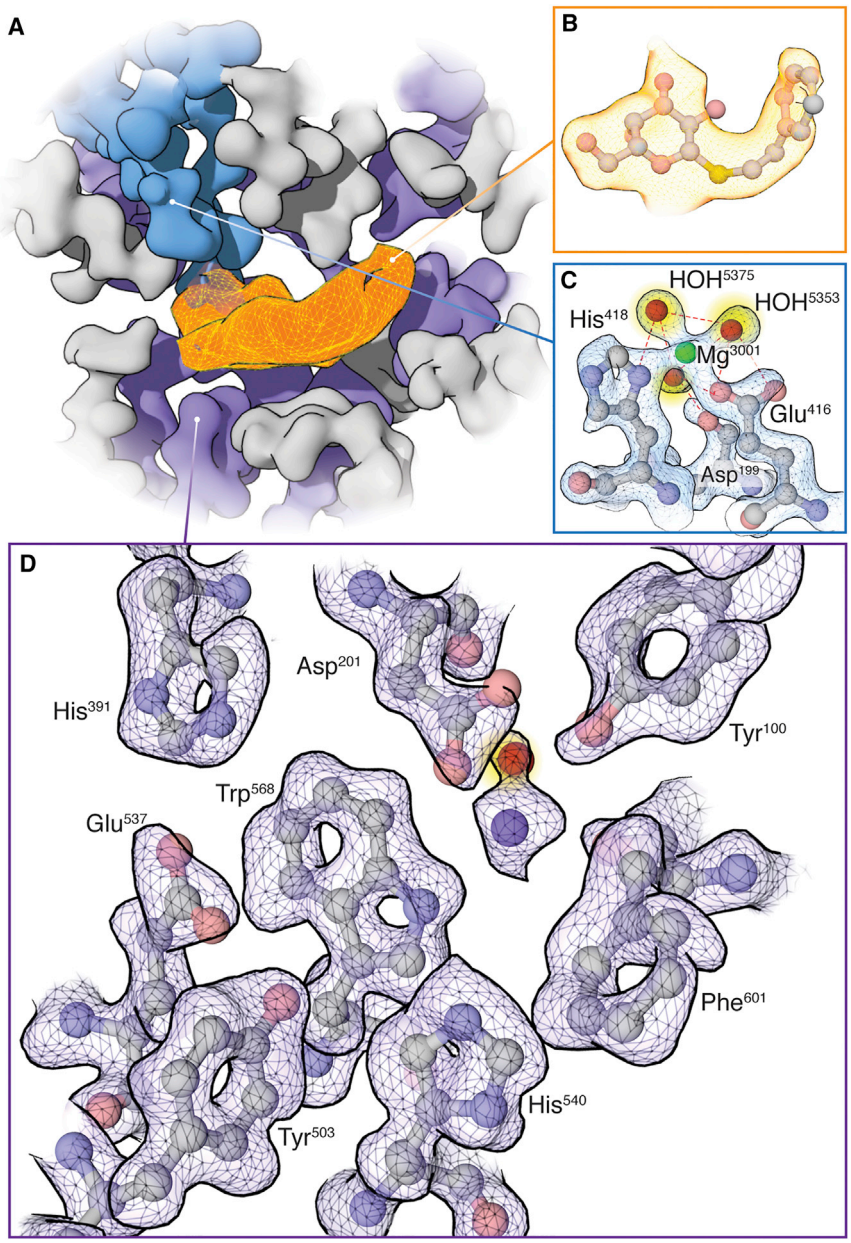

Figure 4. Visualization of the Active Site at Atomic Resolution

(A) Overview of contoured cryo-EM map highlighting density for PETG (orange), Mg^{+} interacting residues (blue), and selected neighboring residues (purple).

(B) Density for the ligand and fitted coordinates showing features consistent with resolutions of ~3–3.5 Å. In (A) and (B), density shown for PETG is from the unsharpened map because sharpening of this region with the same B factor as the rest of the protein leads to increased noise and artifacts due to its lower resolution.

(C) Density for residues in the active site interacting with Mg^{+} (green) and visualization of water molecules (highlighted in yellow).

(D) Close-up view of density map and fitted atomic model for selected active site residues showing delineation of atomic contours.

Related to Video S1.

Quantitative Evaluation of Inhibitor Flexibility

A major motivation in developing methods to improve the resolution of the density map of PETG-bound β-galactosidase was to test whether it could lead also to a significant improvement in resolution of the density for the non-covalently bound inhibitor. Unlike crystal structures that may promote more ordered arrangement of bound ligands, this example of an inhibitor bound to its protein target in the aqueous phase is closer to the physiological context of drug binding. However, as shown in Figure 4, despite the visualization of almost all residues in the active site of the enzyme (Figure 4A) at atomic resolution (Figures 4C and 4D), density for the inhibitor has features whose visual appearance is consistent with much lower resolutions in the range of ~3–3.5 Å (Figure 4B). This suggests that the PETG molecule is likely disordered relative to the rest of the nearby residues in the active site.

of the new density map as compared with the two earlier maps (Figure 3B).

The highest resolution single-particle cryo-EM structure reported to date is that of glutamate dehydrogenase (GDH) at 1.8 Å resolution (Merk et al., 2016). While using a conservative mask that includes the entire β-galactosidase protein yields a similar nominal resolution, the present map displays features at significantly higher resolution in the ordered regions of the protein (Figure S5). Besides the use of our improved image processing strategy, other factors that may have contributed to the improvement in resolution include the fact that β-galactosidase is larger in size (463 kDa versus 334 kDa), is more structurally homogeneous compared with the conformationally dynamic GDH, and the fact that more asymmetric units were used for the reconstruction (601,284 versus 130,908 for GDH).

To gain more insights into the mode of PETG binding, we took advantage of the constraints provided by the cryo-EM density map to obtain a quantitative measure of inhibitor flexibility. Traditional molecular dynamics simulations carried out solely with the coordinates of the structure and force fields can be used to characterize the local fluctuation at each atomic position of the inhibitor. In this "unconstrained" mode of simulation, the median fluctuation for residues within 5 Å of the active site is ~0.39 Å, while median fluctuation for all atoms in PETG is slightly higher at ~ 0.42 Å (Figure 5A). Carrying out the same molecular dynamics simulation by restricting the range of conformational variation of the ligand to those that are allowed within the spread of the experimental cryo-EM density provides an estimate for the

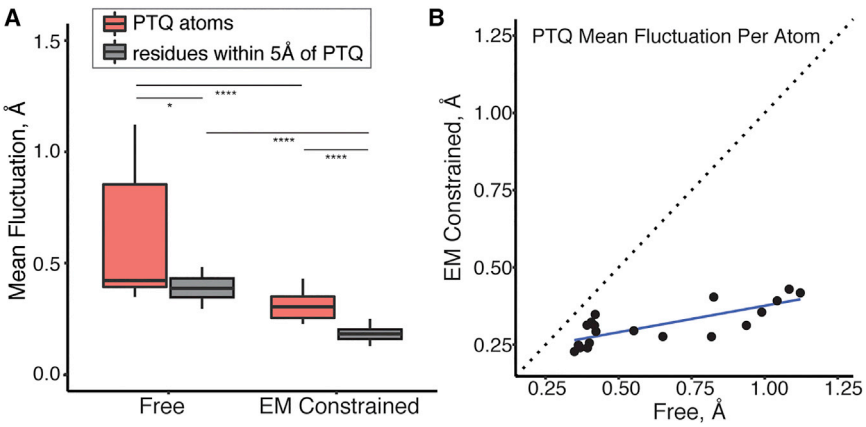

Figure 5. Local Fluctuation of Atomic Positions in Inhibitor and Surrounding Active Site Residues Measured by Molecular Dynamics Simulations

(A) Mean fluctuation in the absence (free) or presence of map constraints (EM constrained) for atomic positions in PETG (referred to as PTQ for consistency with the PDB coordinates; coral), and residues within a 5 Å distance (gray) of the inhibitor. Center crossbar indicates median; boxplot shows quartiles. *$p < 0.05$; ****$p < 0.0001$.

(B) Non-uniform reduction in the per atom fluctuation in PETG inhibitor when measured in the presence of map constraints.

local flexibility that also takes the density map into account. These calculations show that the fluctuation amplitudes for residues within 5 Å of the binding site and atoms of PETG are lowered significantly to distributions with median fluctuation values of ~0.18 Å and ~0.3 Å, respectively (Figure 5A). The reduction in fluctuation at specific atomic positions of the inhibitor with imposition of the constraint of the density map is not uniform (Figure 5B), providing further information on the relative flexibility of different parts of the non-covalently bound ligand.

DISCUSSION

The cryo-EM "revolution" has been fueled in large measure by advances in detector technology and image processing methods (Kühlbrandt, 2014). Here, we show that further resolution improvements are possible with more advanced methods for data processing that make better use of high-quality image data, making it possible to achieve atomic resolution cryo-EM structures. A central piece of our approach is the correction of drift and CTF on a per particle basis. A variety of such strategies have been employed in the past (Abrishami et al., 2015; Grant and Grigorieff, 2015; Rubinstein and Brubaker, 2015; Scheres, 2014; Zhang, 2016; Zheng et al., 2017) but have generally yielded modest improvements in resolution due to the inherent difficulties of dealing with low SNR in small regions of electron micrograph frames. Combination of the incremental effects of local drift and CTF correction with our exposure weighting strategy not only improves resolution but, more importantly, it provides a self-tuning mechanism for optimally extracting high-resolution information present in the raw movie frames. In addition, the increased efficiency in extracting high-resolution information implies that fewer molecular images can be used, thus accelerating the process of structure determination.

FSC-based methods for resolution estimation have been broadly used for cryo-EM structures over the past decade. However, this measure is dependent on the number of particles used to determine the structure and the masks applied to each half-map before computing the correlation. Also, at the resolution ranges relevant to the present discussion, there are systematic differences between atomic models and cryo-EM maps stemming from inaccuracies in the modeling of electron scattering factors and radiation damage effects. Thus, the conventionally used FSC measures between experimentally determined cryo-EM maps and atomic models may in some cases underestimate the true resolution of the cryo-EM maps. Given that high-resolution, and now atomic resolution, cryo-EM maps are becoming a reality, finding approaches to reliably compare resolution values between cryo-EM and X-ray crystallographic approaches will be very important for critical assessment of map quality.

Crystal structures of drug-target complexes are frequently used to identify sites on the drug molecules that can be modified to change specific aspects of the interactions by adding or removing functional groups. The differential measure of flexibility obtained by a combination of atomic resolution cryo-EM density maps and map-constrained simulations reveals the dynamic "footprint" of the binding site and could lead to additional opportunities for improving structure-guided drug discovery.

STAR★METHODS

Detailed methods are provided in the online version of this paper and include the following:

- KEY RESOURCES TABLE
- METHOD DETAILS
  - Data Acquisition and Movie Processing
  - Single Particle Analysis
  - 3D Refinement and Reconstruction
  - Per-particle Frame Alignment
  - Data-Driven Exposure Weighting
  - Per-Particle CTF Estimation
  - Final Map and Structure Refinement
  - Flexibility Analysis of Protein Structures
  - Generation of Figures
- DATA AND SOFTWARE AVAILABILITY

SUPPLEMENTAL INFORMATION

Supplemental Information includes five figures and one video and can be found with this article online at https://doi.org/10.1016/j.str.2018.04.004.

ACKNOWLEDGMENTS

This research was supported by funds from the Center for Cancer Research, National Cancer Institute, NIH, Bethesda, MD (grants ZIA BC 010826, ZIA BC

010278, ZIA BC 010825, and ZIA BC 010827), and utilized the computational resources of the NIH HPC Biowulf cluster (http://hpc.nih.gov). We thank Dr. Alex Wlodawer for providing the anomalous scattering maps of sedolisin and insulin. We dedicate this work to the memory of our colleague Dr. Soojay Banerjee, who sadly passed away during the final stages of the preparation of this manuscript.

AUTHOR CONTRIBUTIONS

Conceptualization, A.B., C.A., S.B., G.S., J.L.S.M., and S.S.; Methodology, A.B., C.A., S.B., N.G., X.W., X.Z., J.L.S.M., and S.S.; Software, A.B., C.A., N.G., and X.W.; Writing, A.B., S.B., L.A.E., X.W., J.L.S.M., and S.S.; Editing, A.B., L.A.E., N.G., J.L.S.M., and S.S.; Visualization, A.B., V.F., and L.A.E.; Supervision, G.S. and S.S.; Project Administration, S.S.; Funding Acquisition, N.G., G.S., and S.S.

DECLARATION OF INTERESTS

The authors declare no competing interests.

Received: December 15, 2017
Revised: March 2, 2018
Accepted: April 5, 2018
Published: May 10, 2018

REFERENCES

Abrishami, V., Vargas, J., Li, X., Cheng, Y., Marabini, R., Sorzano, C., Oscar, S., and Carazo, J.M. (2015). Alignment of direct detection device micrographs using a robust Optical Flow approach. J. Struct. Biol. *189*, 163–176.

Adams, P.D., Afonine, P.V., Bunkóczi, G., Chen, V.B., Davis, I.W., Echols, N., Headd, J.J., Hung, L.-W., Kapral, G.J., Grosse-Kunstleve, R.W., et al. (2010). PHENIX: a comprehensive Python-based system for macromolecular structure solution. Acta Crystallogr. D Biol. Crystallogr *66*, 213–221.

Aguerrebere, C., Delbracio, M., Bartesaghi, A., and Sapiro, G. (2016). Fundamental limits in multi-image alignment. IEEE Trans. Signal Process. *64*, 5707–5722.

Baker, L.A., Smith, E.A., Bueler, S.A., and Rubinstein, J.L. (2010). The resolution dependence of optimal exposures in liquid nitrogen temperature electron cryomicroscopy of catalase crystals. J. Struct. Biol. *169*, 431–437.

Bartesaghi, A., Matthies, D., Banerjee, S., Merk, A., and Subramaniam, S. (2014). Structure of β-galactosidase at 3.2-Å resolution obtained by cryo-electron microscopy. Proc. Natl. Acad. Sci. USA *111*, 11709–11714.

Bartesaghi, A., Merk, A., Banerjee, S., Matthies, D., Wu, X., Milne, J.L., and Subramaniam, S. (2015). 2.2 A resolution cryo-EM structure of beta-galactosidase in complex with a cell-permeant inhibitor. Science *348*, 1147–1151.

Brilot, A.F., Chen, J.Z., Cheng, A., Harrison, S.C., Potter, C.S., Carragher, B., Henderson, R., and Grigorieff, N. (2012). Beam-induced motion of vitrified specimen on holey carbon film. J. Struct. Biol. *177*, 630–637.

Cardone, G., Heymann, J.B., and Alasdair, S.C. (2013). One number does not fit all: mapping local variations in resolution in cryo-EM reconstructions. J. Struct. Biol. *184*, 226–236.

Case, D.A., Betz, R.M., Botello-Smith, W., and Cerutti, D.S. (2016). AMBER 2016 (University of California).

Chen, S., McMullan, G., Faruqi, A.R., Murshudov, G.N., Short, J.M., Scheres, S.H., and Henderson, R. (2013). High-resolution noise substitution to measure overfitting and validate resolution in 3D structure determination by single particle electron cryomicroscopy. Ultramicroscopy *135*, 24–35.

Chen, V.B., Arendall, W.B., Headd, J.J., Keedy, D.A., Immormino, R.M., Kapral, G.J., Murray, L.W., Richardson, J.S., and Richardson, D.C. (2010). MolProbity: all-atom structure validation for macromolecular crystallography. Acta Crystallogr. D Biol. Crystallogr. *66*, 12–21.

Cheng, Y., Grigorieff, N., Penczek, P.A., and Walz, T. (2015). A primer to single-particle cryo-electron microscopy. Cell *161*, 438–449.

Emsley, P., Lohkamp, B., Scott, W.G., and Cowtan, K. (2010). Features and development of Coot. Acta Crystallogr. D Biol. Crystallogr *66*, 486–501.

Glaeser, R.M. (2016). How good can cryo-EM become? Nat. Methods *13*, 28–32.

Goddard, T.D., Huang, C.C., and Ferrin, T.E. (2007). Visualizing density maps with UCSF Chimera. J. Struct. Biol. *157*, 281–287.

Gotz, A.W., Williamson, M.J., Xu, D., and Poole, D. (2012). Routine microsecond molecular dynamics simulations with AMBER on GPUs. 1. Generalized Born. J. Chem. Theory Comput. *8*, 1542–1555.

Grant, T., and Grigorieff, N. (2015). Measuring the optimal exposure for single particle cryo-EM using a 2.6 Å reconstruction of rotavirus VP6. Elife *4*, e06980.

Grant, T., Rohou, A., and Grigorieff, N. (2018). cisTEM, User-friendly software for single-particle image processing. Elife *7*, e35383.

Grigorieff, N. (2016). Frealign: an exploratory tool for single-particle cryo-EM. Methods Enzymol. *579*, 191–226.

Grigorieff, N., Ceska, T.A., Downing, K.H., Baldwin, J.M., and Henderson, R. (1996). Electron-crystallographic refinement of the structure of bacteriorhodopsin. J. Mol. Biol. *259*, 393–421.

Harauz, G., and van Heel, M. (1986). Exact filters for general geometry 3-dimensional reconstruction. Optik *73*, 146–156.

Johnson, G.T., Autin, L., Goodsell, D.S., Sanner, M.F., and Olson, A.J. (2011). ePMV embeds molecular modeling into professional animation software environments. Structure *19*, 293–303.

Kimanius, D., Forsberg, B.O., Scheres, S.H., and Lindahl, E. (2016). Accelerated cryo-EM structure determination with parallelisation using GPUs in RELION-2. Elife *5*, e18722.

Kucukelbir, A., Sigworth, F.J., and Tagare, H.D. (2014). Quantifying the local resolution of cryo-EM density maps. Nat. Methods *11*, 63–65.

Kühlbrandt, W. (2014). Cryo-EM enters a new era. Elife *3*, e03678.

Maier, J.A., Martinez, C., Kasavajhala, K., Wickstrom, L., Hauser, K.E., and Simmerling, C. (2015). ff14SB: improving the accuracy of protein side chain and backbone parameters from ff99SB. J. Chem. Theor. Comput. *11*, 3696–3713.

McDonough, R.N., and Whalen, A.D. (1995). Detection of Signals in Noise, Second Edition (Academic Press).

McMullan, G., Vinothkumar, K.R., and Henderson, R. (2015). Thon rings from amorphous ice and implications of beam-induced Brownian motion in single particle electron cryo-microscopy. Ultramicroscopy *158*, 26–32.

Merk, A., Bartesaghi, A., Banerjee, S., Falconieri, V., Rao, P., Davis, M.I., Pragani, R., Boxer, M.B., Earl, L.A., Milne, J.L., et al. (2016). Breaking cryo-EM resolution barriers to facilitate drug discovery. Cell *165*, 1698–1707.

Pettersen, E.F., Goddard, T.D., Huang, C.C., Couch, G.S., Greenblatt, D.M., Meng, E.C., and Ferrin, T.E. (2004). UCSF Chimera–a visualization system for exploratory research and analysis. J. Comput. Chem. *25*, 1605–1612.

Roe, D.R., and Cheatham, T.E. (2013). PTRAJ and CPPTRAJ: software for processing and analysis of molecular dynamics trajectory data. J. Chem. Theory Comput. *9*, 3084–3095.

Rohou, A., and Grigorieff, N. (2015). CTFFIND4: Fast and accurate defocus estimation from electron micrographs. J. Struct. Biol. *192*, 216–221.

Rosenthal, P.B., and Henderson, R. (2003). Optimal determination of particle orientation, absolute hand, and contrast loss in single-particle electron cryomicroscopy. J. Mol. Biol. *333*, 721–745.

Rubinstein, J.L., and Brubaker, M.A. (2015). Alignment of cryo-EM movies of individual particles by optimization of image translations. J. Struct. Biol. *192*, 188–195.

Scheres, S.H. (2014). Beam-induced motion correction for sub-megadalton cryo-EM particles. Elife *3*, e03665.

Sindelar, C.V., and Grigorieff, N. (2012). Optimal noise reduction in 3D reconstructions of single particles using a volume-normalized filter. J. Struct. Biol. *180*, 26–38.

Wlodawer, A., Li, M., and Dauter, Z. (2017). High-resolution cryo-EM maps and models: a crystallographer's perspective. Structure *25*, 1589–1597.e1.

Wu, X., Brooks, B.R., and Vanden-Eijnden, E. (2016). Self-guided Langevin dynamics via generalized Langevin equation. J. Comput. Chem. *37*, 595–601.

Wu, X., Subramaniam, S., Case, D.A., Wu, K.W., and Brooks, B.R. (2013). Targeted conformational search with map-restrained self-guided Langevin dynamics: application to flexible fitting into electron microscopic density maps. J. Struct. Biol. *183*, 429–440.

Zhang, K. (2016). Gctf: real-time CTF determination and correction. J. Struct. Biol. *193*, 1–12.

Zheng, S.Q., Palovcak, E., Armache, J.-P., Verba, K.A., Cheng, Y., and Agard, D.A. (2017). MotionCor2: anisotropic correction of beam-induced motion for improved cryo-electron microscopy. Nat. Methods *14*, 331–332.

Zwart, P.H., Afonine, P.V., Grosse-Kunstleve, R.W., Hung, L.-W., Ioerger, T.R., McCoy, A.J., McKee, E., Moriarty, N.W., Read, R.J., Sacchettini, J.C., et al. (2008). Automated structure solution with the PHENIX suite. Methods Mol. Biol. *426*, 419–435.

STAR★METHODS

KEY RESOURCES TABLE

REAGENT or RESOURCE	SOURCE	IDENTIFIER
Deposited Data		
Map of β-galactosidase bound to PETG	This paper	EMD-7770
Model of β-galactosidase bound to PETG	This paper	PDB ID 6CVM
Software and Algorithms		
FREALIGN	Grigorieff, 2016	http://cistem.org
CTFFIND4	Rohou and Grigorieff, 2015	http://grigoriefflab.janelia.org/ctf
BLOCRES	Cardone et al., 2013	https://lsbr.niams.nih.gov/bsoft/programs/blocres.html
PHENIX	Adams et al., 2010	https://www.phenix-online.org
COOT	Emsley et al., 2010	http://www2.mrc-lmb.cam.ac.uk/personal/pemsley/coot
MOLPROBITY	Chen et al., 2010	http://molprobity.biochem.duke.edu
AMBER	Case et al., 2016	http://ambermd.org
CPPTRAJ	Roe and Cheatham, 2013	https://github.com/Amber-MD/cpptraj
UCSF Chimera	Goddard et al., 2007	https://www.cgl.ucsf.edu/chimera
ePMV	Johnson et al., 2011	http://epmv.scripps.edu

METHOD DETAILS

Data Acquisition and Movie Processing

The cryo-EM density map described in this work was obtained from the 1,539 movies comprising the publicly available EMPIAR entry 10061. Each movie contains 38 frames recorded every 0.2 s giving an accumulated dose of ~ 45 $e^-/Å^2$ and a total exposure time of 7.6 s. This same dataset was used to determine the previously reported 2.2 Å structure of β-galactosidase (Bartesaghi et al., 2015). Movies were aligned initially using the whole frame alignment technique described earlier (Bartesaghi et al., 2014) and CTF estimation was done with CTFFIND (Rohou and Grigorieff, 2015) using a frequency range for the defocus fit of 30-3.5 Å.

Single Particle Analysis

298,715 particles were picked automatically using a Gaussian disk of 80 Å in radius (using a less stringent peak thresholding criteria than that used to obtain the 2.2 Å structure), extracted using a binning factor of 8 corresponding to 2.55 Å per pixel, and subjected to 3D refinement in FREALIGN (Grigorieff, 2016). A bimodal distribution of FREALIGN scores was observed and only the 150,321 particles assigned to the lobe with the highest scores were kept for further processing. These particles were then re-extracted from the original micrographs using a binning factor of 2 equivalent to 0.64 Å per pixel (box size of 768x768 pixels), and subjected to an additional 8 rounds of local refinement. D2 symmetry was imposed throughout processing. The highest resolution information used during all stages of refinement carried out in FREALIGN was set to 2.8 Å. The resulting map, which uses the full 45 $e^-/Å^2$ exposure served as a starting point to evaluate the improvements from each of the image processing advances we introduce in the present work. The nominal resolution of this map is 2.3 Å (0.143-cutoff FSC criterion; Figures S1C and S1D, blue curves), which is slightly lower than the previously reported 2.2 Å map which had fewer particles (~40,000) and only used a subset of the data (frames 4-13) to minimize loss of high-resolution information from image drift and radiation damage.

3D Refinement and Reconstruction

All refinement and reconstruction operations were done with a new version of FREALIGN that uses a matched filter to align particle images. This requires noise-whitening of the particle images based on the noise power spectrum, which is estimated in FREALIGN as the average power spectrum of the particle images outside a specified particle radius. The signal power in the images is estimated using the particle spectral signal-to-noise ratio derived from resolution statistics of the current best reconstruction (Sindelar and Grigorieff, 2012). For the matched filter, the signal in the reference projections is amplitude-scaled to match the predicted signal in the image to be aligned, and the projection direction and x,y translation is then adjusted to maximize the correlation coefficient between image and reference. Improvements to FREALIGN further include speed optimization by on-the-fly real-space image cropping and pixel binning through Fourier cropping where appropriate, as well as the use of processor-optimized libraries. The improved version of FREALIGN is part of cisTEM (www.cistem.org), a new image processing software for single particle averaging (Grant et al., 2018).

Per-particle Frame Alignment

To overcome the challenges of dealing with the very low SNR present in the small image area of single particle frames (Aguerrebere et al., 2016), we follow the movement of individual particles throughout the exposure using a strategy similar to the "particle-polishing" procedure (Scheres, 2014). Frames for each particle were extracted from the aligned micrographs (after whole-frame alignment), and *weighted* running averages for each particle were obtained and re-aligned to projections of the refined 3D model. This produced a set of noisy trajectories for the movement of each particle, which were then regularized using spatio-temporal smoothness constraints. The resulting alignments were used to update the running frame averages for each particle and were re-aligned once again to the 3D reference. Repeating this process until convergence (typically 10 iterations), resulted in the final assignment of local particle trajectories as shown in Figures 1A–1C. Compared to the 2.3 Å map obtained using whole-frame alignment, resolution after doing per-particle drift correction using this approach improved by 0.09 Å, Figure S1C (middle).

To compute the running averages of frames we used Gaussian weights with a variance equivalent to 20% the number of frames in each movie, meaning that only the closest ~15 frames (7 before and 7 after) have non-zero contributions to each running average. Re-alignment of the running averages to the 3D reference was implemented using FREALIGN by only allowing translational movements while keeping particle orientations fixed at the values obtained during the initial 3D refinement. To regularize the local trajectories, we averaged the movement of nearby particles using weights drawn from a Gaussian distribution based on the distance between particles (variance of 16 nm), followed by fitting of cubic splines to the *net* particle trajectories obtained by composing the whole-frame movement with the local drift component. Application of this strategy to particles with lower molecular weight than β-galactosidase may require the use of Gaussians with wider variances, both for the computation of running frame averages and regularization of trajectories, in order to compensate for the reduction in image contrast produced by smaller-sized complexes.

Data-Driven Exposure Weighting

Correlation scores assigned to individual frames of every particle were averaged across each micrograph resulting in 1D score-exposure curves (Figure 1D). Corresponding 2D frequency weights (Figure 1E) were derived using the formula $w(f,s) = e^{-\frac{1}{2}r(f)^4 y(s)} / \sum_f w(f,s)$, where f denotes the frame number and s the spatial frequency. The dependency on the normalized score-averages, $0 \leq \overline{pr(f)} \leq 1$, was set to $r(f) = \left(1 - \overline{pr(f)}^4\right)$ to prevent a few top scoring frames from dominating the average in the high-frequency regime, and the frequency modulation was set empirically to $y(s) = e^{7.62s}$. For micrographs containing fewer than 10 particles the score averages were too noisy to be reliable, and instead the mean score-exposure curve obtained by averaging across all micrographs in the dataset was used for weighting (Figure S1A). Compared to using the full unweighted 45 $e^-/Å^2$ exposure to obtain the baseline 2.3 Å map, the improvement in map resolution using the proposed exposure weighting scheme was 0.12 Å, Figure S1C (right).

Per-Particle CTF Estimation

Initial 3D refinement was carried out with the standard approach of using global defocus/astigmatism parameters for each micrograph estimated using CTFFIND. To account for spatial variations of the CTF within each image, defocus/astigmatism estimation was done on a per particle basis using a strategy similar to that implemented in GCTF (Zhang, 2016). At every particle position, *weighted* averages of power spectra of neighboring particles were obtained and subjected to CTF estimation using CTFFIND (option –amplitude-spectrum-input), resulting in a smooth distribution of CTF parameters, Figure 1A. Weights were derived from a Gaussian distribution based on the inter-particle distances using a variance of 32 nm. Compared to the 2.3 Å reconstruction that used per-micrograph defocus parameters, the use of local CTF measurements resulted in an improvement in resolution of 0.07 Å, Figure S1C (left).

Final Map and Structure Refinement

Combination of the local drift correction, exposure weighting and local CTF estimation strategies resulted in an improved map that was iteratively refined in FREALIGN. A negative B-factor was applied to the final map followed by application of a soft shape mask obtained by thresholding the unsharpened density map followed by apodization. Coordinates of one beta-galactosidase protomer with 2 sodium ions, 2 magnesium ions and a 2-phenylethyl 1-thio-beta-D-galactopyranoside extracted from the 2.2 Å resolution structure (Chain A of PDB ID 5A1A) was fitted onto the new cryo-EM map. The backbone of the starting model was manually adjusted in COOT followed by five cycles of real space refinement in PHENIX (Zwart et al., 2008). About 400 water molecules were then modeled at peaks of protein-masked density above 2.0 r.m.s.d. and with distance to protein atom between 2.5 and 3.5 Å. About 600 additional water molecules were placed manually. D2 symmetry was applied on the protomer to generate the whole tetramer of beta-galactosidase. Water molecules at interface of protomers were manually edited to avoid interatomic clashes. Gln, Asn and His sidechains were automatically flipped using MOLPROBITY's Reduce (Chen et al., 2010) and then manually checked. Finally, three cycles of real space refinement were performed for the whole tetramer in PHENIX.

Flexibility Analysis of Protein Structures

The refined tetramer structure of β-galactosidase was simulated using the AMBER package (Case et al., 2016) to examine conformational flexibility of the system. The map-restrained self-guided Langevin dynamics (MapSGLD) (Wu et al., 2013) was used to apply map restraints of the following form:

$$E_{map} = -c_{map}\sum_{a}^{N} m_a \widehat{\rho}(x_a, y_a, z_a) \quad \text{(Equation 1)}$$

Which correlates atomic mass, m_a, with the normalized map density at the atom position, $\widehat{\rho}(x_a,y_a,z_a)$. The restraint constant, c_{map}, sets the strength of the map-restraint. The units of m_a and c_{map} are g/mol and kcal/g, respectively. Equation (1) produces an energy landscape in the shape of the density distribution, $-c_{map}\widehat{\rho}(x_a,y_a,z_a)$, for every restrained atom, a. It induces atoms to move to positions of lower energy, or of higher density. The restraint constant is set to $c_{map} = 0.1\ kcal/g$. The map restraint coupled with the AMBER ff14SB force field (Maier et al., 2015), as well as the generalized Born solvation model (Gotz et al., 2012), makes the desired structure the global minimum. An improved conformational sampling method, self-guided Langevin dynamics via generalized Langevin equation (SGLD-GLE) (Wu et al., 2016), was applied to achieve enhanced conformational sampling while maintaining the correct canonical ensemble distribution. The local averaging time and the guiding factor were 0.2 ps and 1, respectively. The MapSGLD simulations were 1 ns in length with a time step of 1 fs. The conformations were saved every 10 ps for post simulation analysis. AMBER trajectory post analysis was done with Cpptraj (Roe and Cheatham, 2013). Fluctuations of residues and atoms were averaged over the four copies of the tetramer. Statistical differences between groups were calculated with the Wilcoxon rank sum test, and p-values were adjusted for multiple comparisons with the Bonferroni correction. Correlation between mean fluctuation values for unconstrained versus EM-constrained PETG atoms was evaluated using Kendall's *tau*.

Generation of Figures

Figures of map density and coordinates were created in UCSF Chimera (Pettersen et al., 2004) and Maxon Cinema4D, except for the individual residue images from the 2.2 Å cryo-EM map, which were created in UCSF Chimera. For the images created in Maxon Cinema4D, the coordinates were imported using the Cinema4D plugin Embedded Python Molecular Viewer (ePMV) (Johnson et al., 2011).

DATA AND SOFTWARE AVAILABILITY

The accession numbers for the map and corresponding atomic model reported in this paper are EMD-7770 and PDB ID 6CVM.

Structure, Volume *26*

Supplemental Information

Atomic Resolution Cryo-EM Structure of β-Galactosidase

Alberto Bartesaghi, Cecilia Aguerrebere, Veronica Falconieri, Soojay Banerjee, Lesley A. Earl, Xing Zhu, Nikolaus Grigorieff, Jacqueline L.S. Milne, Guillermo Sapiro, Xiongwu Wu, and Sriram Subramaniam

SUPPLEMENTARY FIGURES

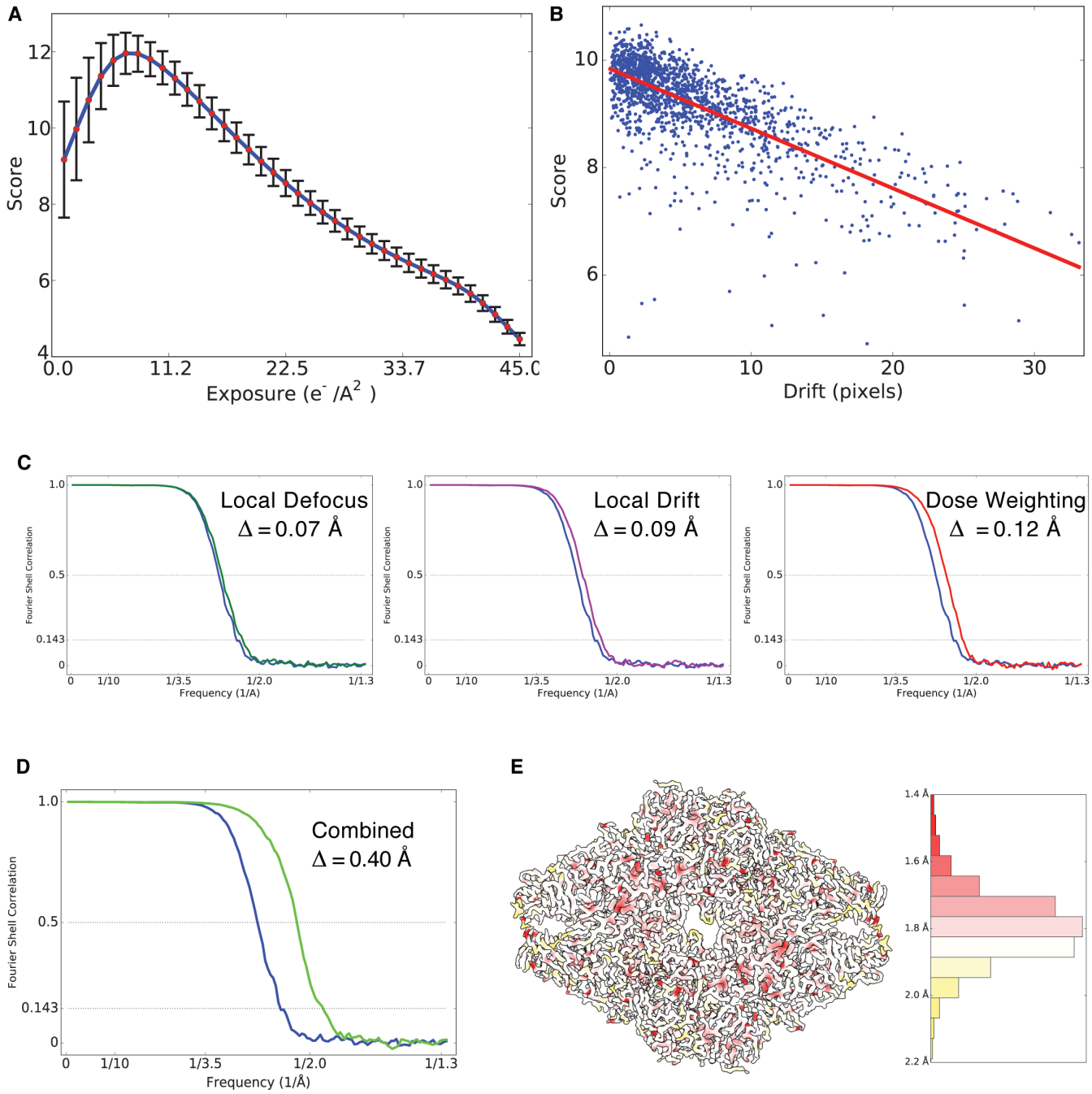

Supplementary Figure 1. Data-driven dose weighting strategy based on per-particle FREALIGN score measurements and improvement in map resolution according to Fourier Shell Correlation (FSC) and local resolution metrics. Related to Figures 1 and 2.
A) Average score values across all particles in dataset plotted as a function of the cumulative electron exposure. Vertical bars indicate the variance across all measurements, showing larger values at the beginning of the exposure and smaller values towards higher accumulated doses. **B)** Scatter plot of average score values assigned to the first frame of each movie versus amount of initial drift (scores were

averaged across all particles in each movie and initial drift was measured between the first two frames of each movie using super-resolution pixel units). Red line indicates a linear fit to the data showing an inverse correlation between the amount of drift and the average score value. **C)** Resolution improvement from each of the processing components of our strategy with respect to the 2.3 Å baseline reconstruction obtained using global frame alignment, global CTF estimation and the full exposure (blue curves). FSC curves between half-maps for reconstructions obtained using only local defocus correction (left, green curve), only local drift correction (middle, magenta curve), and only data-driven dose weighting (right, red curve), corresponding to resolution improvements of 0.07 Å, 0.09 Å, and 0.12 Å, respectively. **D)** Half-map FSC curve for the final reconstruction obtained by combining all three components of our approach, showing an overall resolution improvement of 0.4 Å (green curve, ~1.9 Å by 0.143 criterion) with respect to the 2.3 Å baseline reconstruction (blue curve). **E)** Color-coded cut-out surface representation of the β-galactosidase tetramer and corresponding 1D histogram showing local resolution values ranging from 2.2 Å to 1.4 Å in different regions of the protein measured by BLOCRES (Cardone et al., 2013).

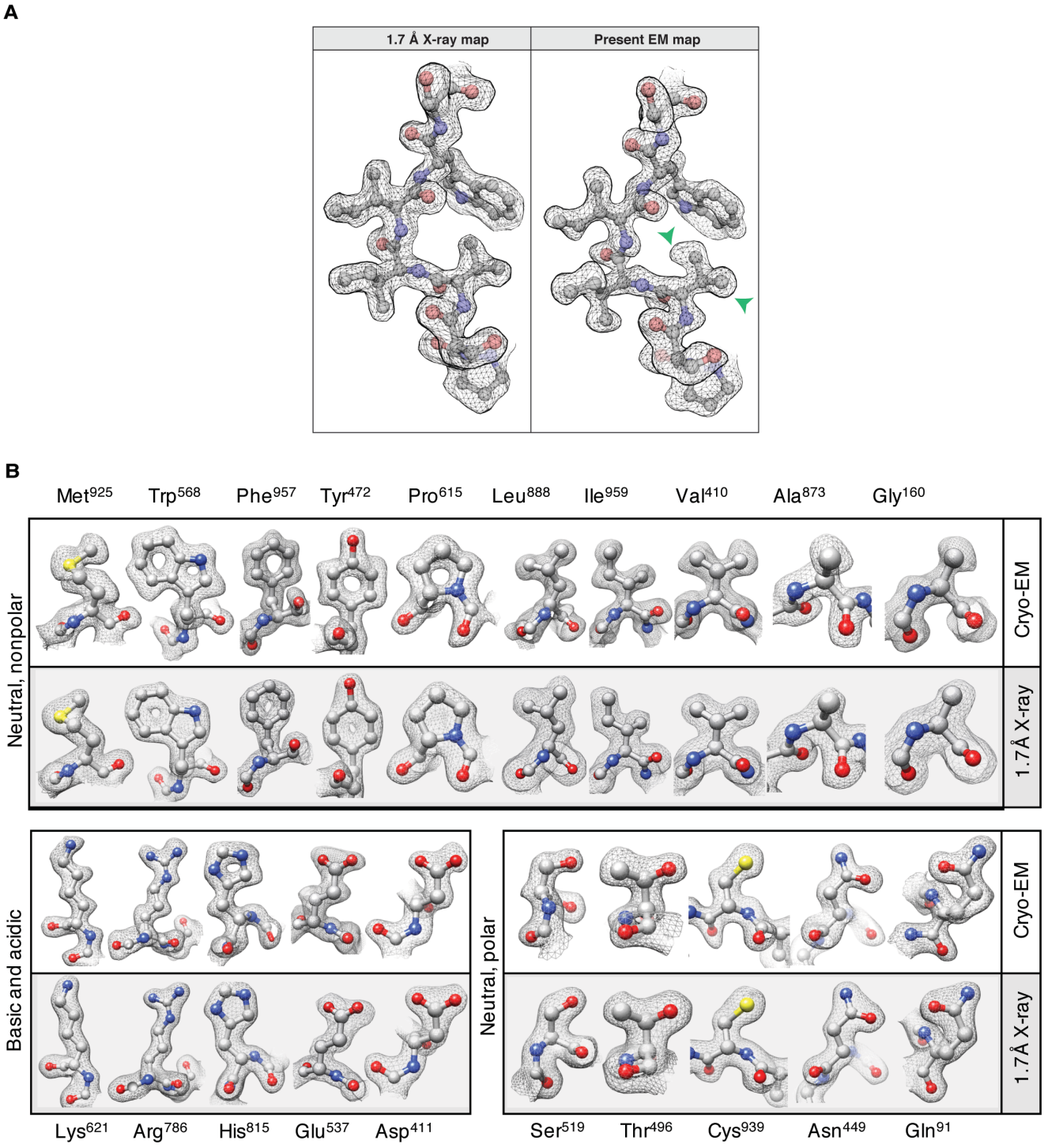

Supplementary Figure 2. Comparison of cryo-EM density map with 1.7 Å X-ray structure. Related to Figure 2.

A) Side-by-side comparison of region spanning residues 451- 457 between the 2Fo-Fc map computed from the 1.7 Å resolution X-ray structure (PDB ID 1DP0) and the new map. Green arrowheads highlight examples where the new cryo-EM map shows well-resolved outlines for individual atoms. **B)** Side-by-side comparison of density for each of the 20 amino acids between the X-ray and the cryo-EM maps.

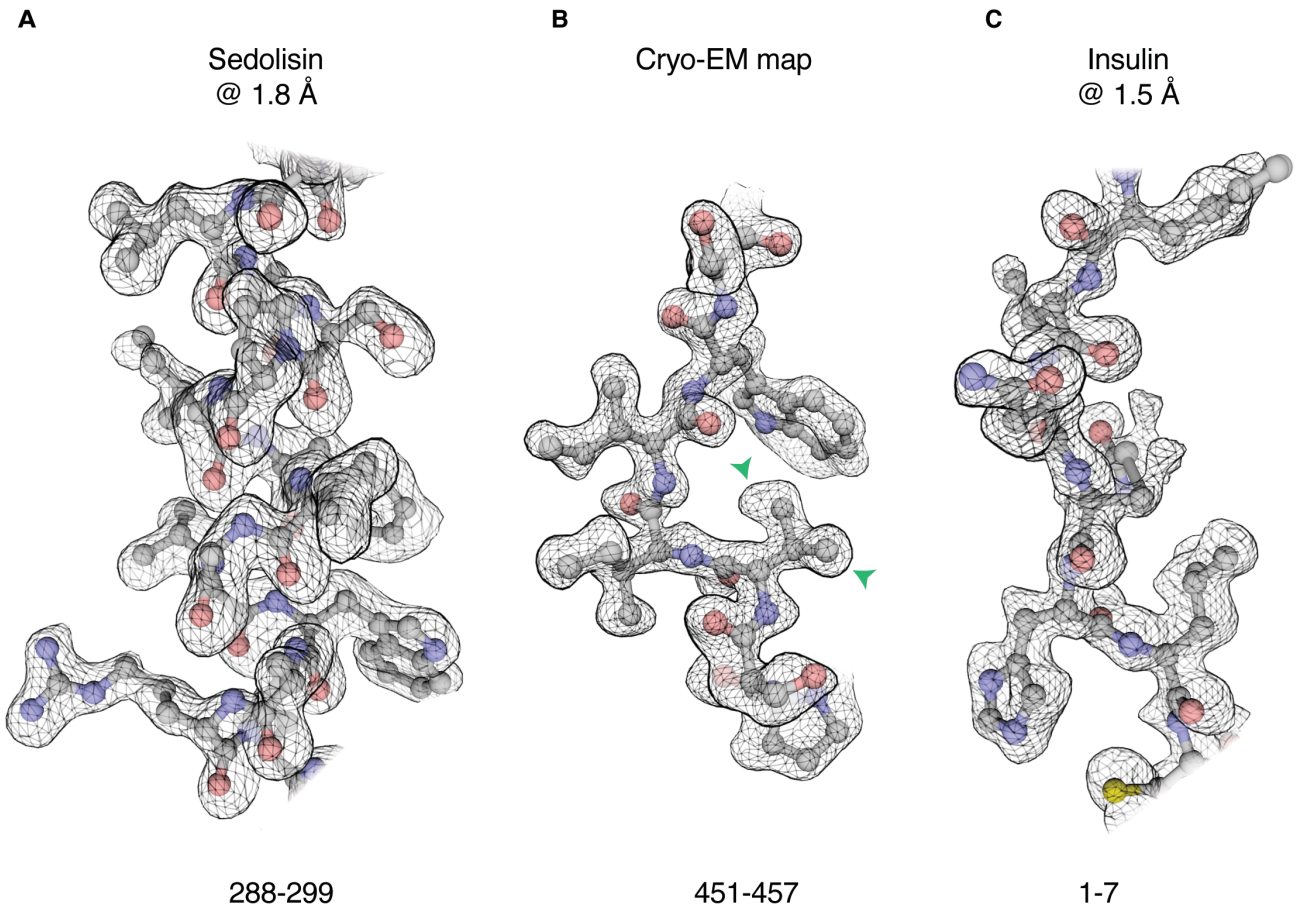

Supplementary Figure 3. Comparison of cryo-EM density map with 1.8 Å and 1.5 Å resolution X-ray maps obtained by anomalous scattering. Related to Figure 2.
Comparison of representative density features observed in the X-ray map of sedolisin at 1.8 Å resolution (residues 288-299, left), our cryo-EM map (residues 451-457, center) and the X-ray map of insulin at 1.5 Å resolution (residues 1-7, right). A qualitative evaluation of the delineation of punctate densities for non-H atoms suggest that the features observed in the most well-ordered regions of the cryo-EM density map are better resolved than in the 1.8 Å map of sedolisin and compare favorably with those seen in the 1.5 Å electron density map of insulin.

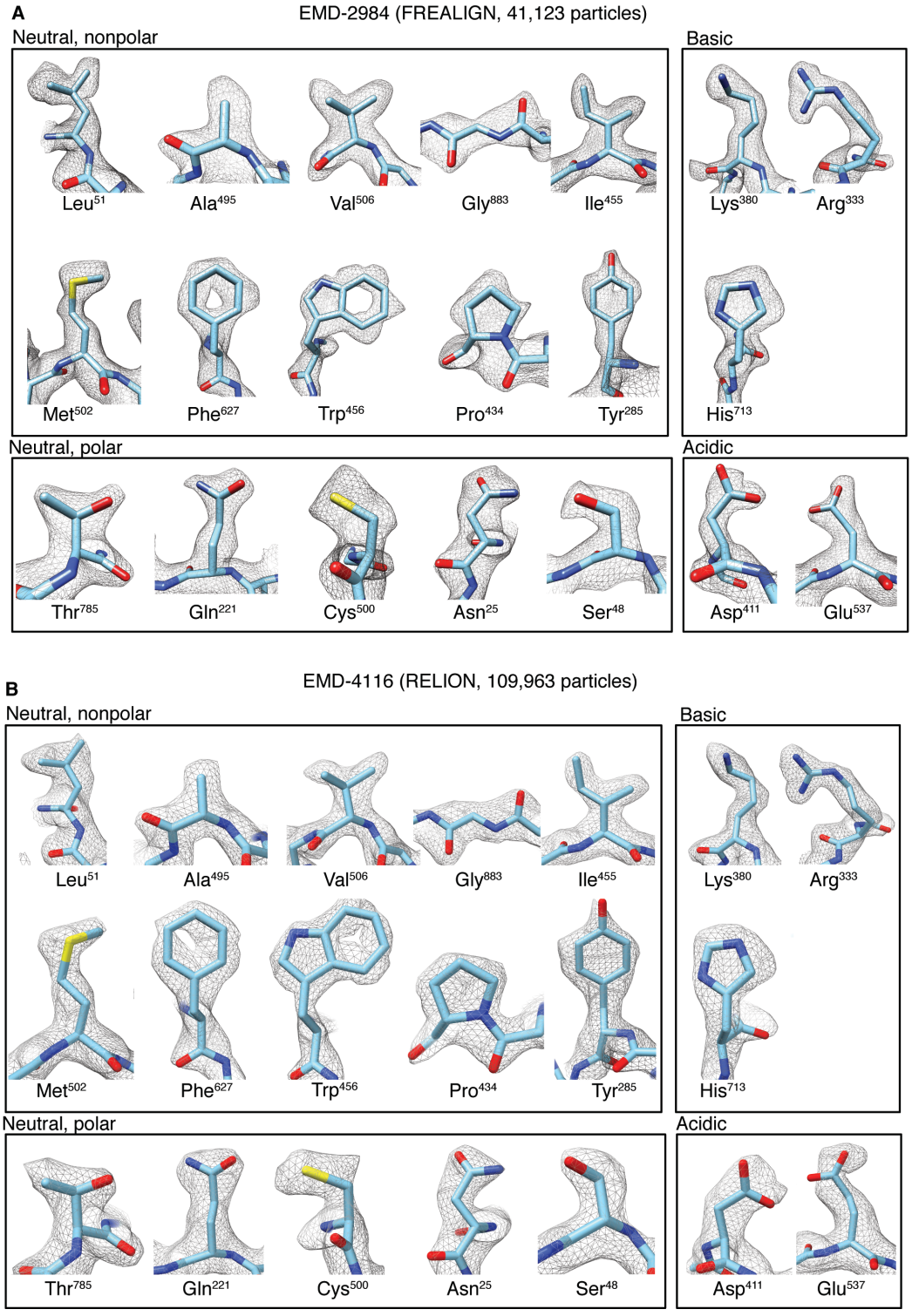

Supplementary Figure 4. Comparison of features between our previous 2.2 Å map and the RELION map. Related to Figure 3.

A-B) Side-by-side comparison of 20 amino acid panels as presented in Figure 4 of (Bartesaghi et al., 2015) between the previously published 2.2 Å map EMD-2984 obtained from ~40,000 particles (**A**), and map EMD-4116 obtained by Scheres and co-workers using RELION from ~110,000 particles (**B**).

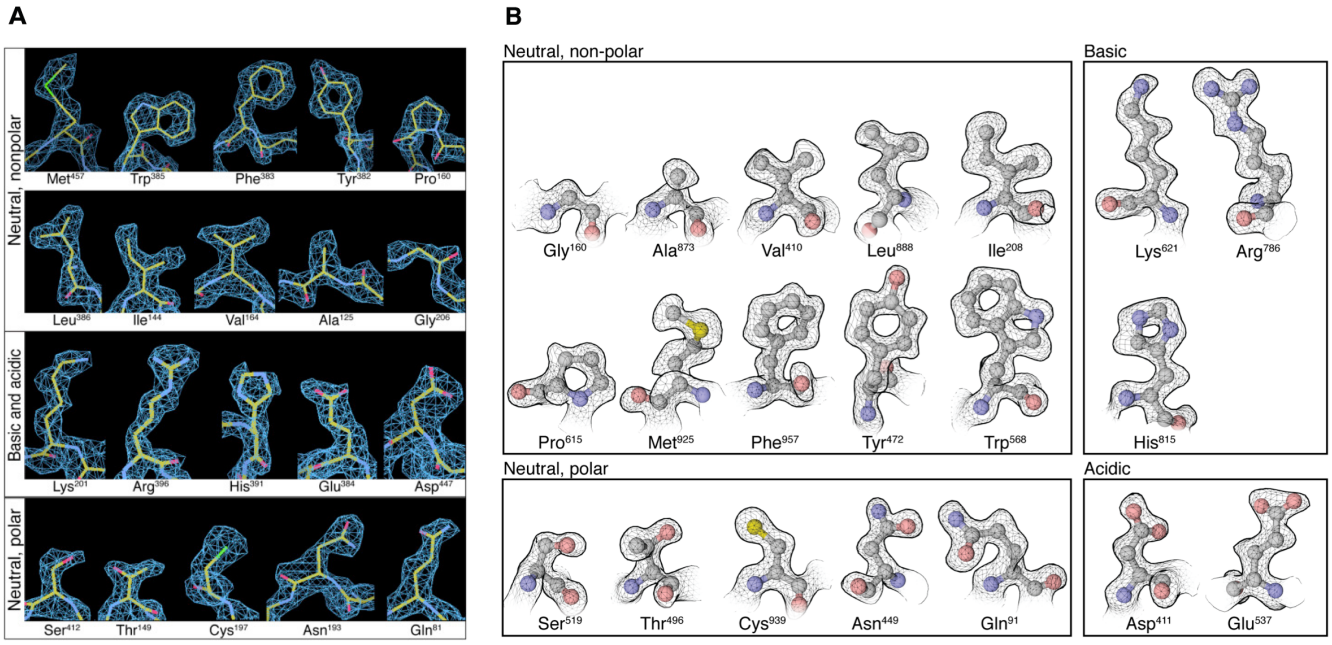

Supplementary Figure 5. Comparison between the previously reported 1.8 Å map of glutamate dehydrogenase (GDH) and the present map. Related to Figure 2.
A-B) Side-by-side comparison of 20 amino acid panels from the 1.8 Å resolution map of GDH (reproduced from Figure 4 (Merk et al., 2016)) (**A**), and the present map of β-galactosidase (reproduced from Figure 2c) (**B**).